Science Advances
AAAS

advances.sciencemag.org/cgi/content/full/6/10/eaay2324/DC1

Supplementary Materials for

The spin Hall effect of Bi-Sb alloys driven by thermally excited Dirac-like electrons

Zhendong Chi, Yong-Chang Lau*, Xiandong Xu, Tadakatsu Ohkubo, Kazuhiro Hono, Masamitsu Hayashi*

*Corresponding author. Email: yongchang.lau@qspin.phys.s.u-tokyo.ac.jp (Y.-C.L.); hayashi@phys.s.u-tokyo.ac.jp (M.H.)

Published 6 March 2020, *Sci. Adv.* **6**, eaay2324 (2020)
DOI: 10.1126/sciadv.aay2324

This PDF file includes:

Section S1. STEM results of films

We performed high-angle annular dark-field scanning transmission electron microscopy (HAADF-STEM) analysis of samples using a FEI Titan^{TM} G2 80-200 transmission electron microscope with a probe forming aberration corrector operated at 200 kV. Samples were cross-sectioned into thin lamellae by focused ion beam (FIB) lift-out technique using FEI Helios G4 UX. Nanobeam electron diffraction patterns were taken with a 10-μm-diamter condenser aperture. Element-selected analysis were carried out via energy-dispersive X-ray spectroscopy (EDS)[61].

Figure S1(a) shows a HAADF-STEM image and the corresponding EDS maps of one of the heterostructures with 10.9 $Bi_{0.53}Sb_{0.47}$/2 CoFeB. EDS line scans averaged over the entire image (19 $\times$ 26 nm^2) are shown in Fig. S1(b). We find that Sb tends to diffuse toward the CoFeB layer. This may be attributed to the finite solubility of Sb in Co and Fe, in contrast to Bi which is practically immiscible with any of these elements.

Section S2. Magnetic properties of BiSb/CoFeB

Magnetic moments of the heterostructures were measured using a vibrating sample magnetometer (VSM) at room temperature. A superconducting quantum interference device (SQUID) is used to measure the temperature dependence of the magnetic properties. The magnetization hysteresis loops of a heterostructure with 5.6 $Bi_{0.53}Sb_{0.47}$/2 CoFeB are displayed in Fig. S2(a) under an external magnetic field applied parallel and perpendicular to film plane. The magnetic easy axis of the CoFeB layer points along the film plane.

The t_{CoFeB} dependence of the saturated magnetic moment of heterostructures with two different $Bi_{0.53}Sb_{0.47}$ layer thicknesses are plotted in Fig. S2(b). Data from the two series are hardly discernable. We therefore assume that the saturation magnetization M_s and the magnetic dead layer thickness t_{D} of the CoFeB layer are independent of the $Bi_{1-x}Sb_x$ thickness. Linear fit to all the data are shown in Fig. S2(b) as the solid line. From the slope and the x-intercept of the linear line, M_s and t_{D} are determined to be 1190 ± 20 emu/cm^3 and 0.46 ± 0.04 nm, respectively. In Fig. S2(b), we also show M_s values of heterostructures with 10 Bi/2 CoFeB and 10 Sb/2 CoFeB. As we find almost no difference in M_s when the Sb concentration is changed, we assume a constant M_{s} and t_{D} for all heterostructures studied (with different x).

Figure S2(c) shows the magnetization hysteresis loops of the same heterostructure shown in (a) evaluated at 300 K and 10 K. A SQUID magnetometer is used: the field is applied along the film plane. The two loops measured at 300 K and 10 K overlap. We thus assume the temperature has little influence on $M_{\rm s}$ of CoFeB for all samples.

Section S3. Anomalous Hall resistance and anisotropy field

The Hall resistance $R_{\rm xy}$ of the heterostructures are measured using a dc current of 20 μA. An exemplary loop of $R_{\rm xy}$ vs. H_z is displayed in Fig. S3(a). The slope of $R_{\rm xy}$ at large magnetic field is attributed to the ordinary Hall effect of BiSb. Data at large magnetic field is fitted using a linear function. The anomalous Hall resistance $R_{\rm AHE}$ is obtained from the y-axis intercept of the fitted linear function shown by the red dotted lines[42]. The low field data are also fitted with a linear function, as shown by the blue dotted line. The out-of-plane anisotropy field $H_{\rm K}$ is determined by the x-intercept of the two linear functions: see Fig. S3(a) for an illustration to obtain $H_{\rm K}$ from the loop.

Figure S3(b) and (e) show the layer thickness dependence of $R_{\rm AHE}$ and $H_{\rm K}$, respectively. As evident, $|R_{\rm AHE}|$ decreases with increasing $Bi_{1-x}Sb_x$ thickness regardless of the size of $t_{\rm CoFeB}$ (Fig. S3(b)), which is attributed to current shunting into the $Bi_{1-x}Sb_x$ layer. Figure S3(e) shows that $H_{\rm K}$ is nearly independent of the $Bi_{1-x}Sb_x$ layer thickness. $H_{\rm K}$ increases with decreasing CoFeB layer thickness, which is consistent with the presence of a perpendicular magnetic anisotropy at the CoFeB/MgO interface[62]. The Sb concentration (x) dependence of $R_{\rm AHE}$ and $H_{\rm K}$ are displayed in Fig. S3(c) and S3(f), respectively. We find $|R_{\rm AHE}|$ decreases with increasing Sb concentration, which is predominantly due to larger current shunting into the $Bi_{1-x}Sb_x$ layer as the layer conductivity increases with increasing x (see Fig. 3(a)). $H_{\rm K}$ tends to increase with increasing x. Although the underlying mechanism is not clear, these results indicate that the perpendicular magnetic anisotropy, predominantly defined at the CoFeB/MgO interface, is influenced by the underlayer[63]. The temperature dependence of $R_{\rm AHE}$ and $H_{\rm K}$ for heterostructures with 10 $Bi_{1-x}Sb_x$/2 CoFeB are shown in Fig. S3(d) and (g), respectively. For all x studied, both $|R_{\rm AHE}|$ and $H_{\rm K}$ tend to increase with decreasing temperature. Changes in $R_{\rm AHE}$ are mainly attributed to the different temperature dependence of the conductivity of $Bi_{1-x}Sb_x$ and CoFeB. Whereas the conductivity of CoFeB is practically independent of the temperature, that of $Bi_{1-x}Sb_x$ de-

creases with decreasing temperature, resulting in redistribution of the current within the two layers on varying the temperature. The increase of H_{K} with temperature is unclear and requires further investigation.

Section S4. First harmonic Hall resistance of BiSb/CoFeB

Exemplary results of the first harmonic Hall resistance $R_{1\omega}$ plotted against the angle φ_{H} (the angle between the external magnetic field applied along the film plane and the x axis) are shown in Fig. S4(a). The results can be fitted using the following function

$$R_{1\omega} = R_{\mathrm{PHE}} \sin 2\varphi_{\mathrm{H}} + \zeta R_{\mathrm{AHE}} \cos \varphi_{\mathrm{H}} \tag{S4}$$

where ζ is a constant that is introduced to take into account an unintentional misalignment between the external magnetic field and the film plane. We use Eq. (S4) to obtain the planar Hall resistance R_{PHE}. We find little change in $R_{1\omega}$ on varying the magnetic field, suggesting good sample alignment and weak external field dependence of R_{PHE}. We therefore take the average R_{PHE} obtained under different magnetic fields.

Figure S4(b) illustrates the $\mathrm{Bi}_{1-x}\mathrm{Sb}_x$ and CoFeB layer thickness dependence of R_{PHE}. Note that in heavy metal/CoFeB bilayers R_{PHE} contains contribution from the spin Hall magnetoresistance (SMR)[64, 65]. We find a peak in $|R_{\mathrm{PHE}}|$ at $t_{\mathrm{BiSb}} \sim 5$ nm, which is approximately twice of the $\mathrm{Bi}_{1-x}\mathrm{Sb}_x$ spin diffusion length (~ 2.3 nm) determined in the main text. The position of the peak in $|R_{\mathrm{PHE}}|$ is consistent with the SMR theory[18]. R_{PHE} for heterostructures with 10 $\mathrm{Bi}_{1-\mathrm{x}}\mathrm{Sb}_{\mathrm{x}}$/2 CoFeB are plotted as a function of Sb concentration (x) and temperature in Fig. S4(c) and S4(d) respectively. We consider these changes are mainly due to variation of the spin Hall efficiency and current redistribution within the bilayers.

Section S5. Two-band model analysis of BiSb

Carrier concentration and mobility of $\mathrm{Bi}_{1-x}\mathrm{Sb}_x$ are estimated based on a classical two-carrier model, *i.e.* both electrons and holes contribute to the transport. Experimental inputs of the model are: Hall coefficient R_{H} (given by $R_{\mathrm{H}} = R_{xy} t_{\mathrm{BiSb}}/H_z$, where H_z represents H_{ext} along the z-axis), longitudinal conductivity at zero field σ_{BiSb} and the quadratic component

of the transverse magnetoresistance (MR) with H_z. The equations read[66]

$$R_{\mathrm{H}} = \frac{(n_e\mu_e^2 - n_h\mu_h^2) + (n_h - n_e)\mu_h^2\mu_e^2 H_z^2}{e\left(n_h\mu_h + n_e\mu_e\right)^2 + (n_h - n_e)^2\mu_h^2\mu_e^2 H_z^2} \tag{S5}$$

$$\sigma_{\mathrm{BiSb}} = e\left(n_h\mu_h + n_e\mu_e\right) \tag{S6}$$

$$\mathrm{MR} = \frac{\rho_{\mathrm{BiSb}}\left(H_z\right) - \rho_{\mathrm{BiSb}}\left(H_z = 0\right)}{\rho_{\mathrm{BiSb}}\left(H_z = 0\right)} = \frac{\mathrm{n_h}\mu_{\mathrm{h}}\mathrm{n_h}\mu_{\mathrm{h}}\left(\mu_{\mathrm{h}} + \mu_{\mathrm{e}}\right)^2 H_z^2}{\left(\mathrm{n_h}\mu_{\mathrm{h}} + \mathrm{n_e}\mu_{\mathrm{e}}\right)^2 + \left(\mathrm{n_h} - \mathrm{n_e}\right)^2\left(\mu_{\mathrm{h}}\mu_{\mathrm{e}}\right)^2 H_z^2} \tag{S7}$$

Here, $n_h(n_e)$ and $\mu_h(\mu_e)$ denote the carrier density and the mobility of hole(electron), respectively. Since Bi and Sb have the same number of p valence electrons, we assume $n_h \approx n_e \equiv n$ for all x of $\mathrm{Bi_{1-x}Sb_x}$. With such carrier compensation, Eqs. (S5), (S5) and (S5) can be reduced to

$$R_{\mathrm{H}} = \frac{ne\left(\mu_e^2 - \mu_h^2\right)}{\sigma_{\mathrm{BiSb}}^2} \tag{S8}$$

$$\sigma_{\mathrm{BiSb}} = ne\left(\mu_h + \mu_e\right) \tag{S9}$$

$$\mathrm{MR} = \mu_{\mathrm{e}}\mu_{\mathrm{h}}H_z^2 = \beta H_z^2 \tag{S10}$$

Based on these equations, n and mobilities μ_h, μ_e can be estimated from experimental results. As an example, the temperature dependences of R_{xy} and MR for 10 $\mathrm{Bi_{0.83}Sb_{0.17}}$ grown on Ta seed layer are shown in Fig. S5(a) and S5(b). R_{H} and $\beta \equiv \mu_e\mu_h$ extracted from the plots are shown in Fig. S5(c) and S5(d), respectively. The large quasi-linear MR at 10 K is mainly attributed to the weak anti-localization of $\mathrm{Bi_{1-x}Sb_x}$ exhibiting strong spin orbit coupling. We therefore limit our analysis of carrier density and mobility to temperature ranging from 50 K to 300 K. The estimated n, μ_h and μ_e are shown in Fig. 5 of the manuscript.

Section S6. Evaluation of the SOT analysis protocol

To verify the analysis protocol used here, the damping-like and field-like SOTs for a standard sample, Sub./1 Ta/3.3 Pt/2 CoFeB/2 MgO/1 Ta (thicknesses in nm) heterostructure, was measured. Figure S6(a) shows the resistivity of Pt (ρ_{Pt}) as a function of temperature. A parallel circuit model is employed to estimate the resistivity of Pt; we assume the only other conducting layer is CoFeB, which has a resistivity of $\rho_{\mathrm{CoFeB}}\sim$140 $\mu\Omega$cm. We find ρ_{Pt} is $\sim$44 $\mu\Omega$cm at room temperature and decreases to $\sim$38 $\mu\Omega$cm at 5 K, reflecting the metallic transport property of Pt (the small residual-resistance ratio indicates large amount of impurity in Pt). Parameter A at 300K, which is defined in Eq. (2) of the main text, is plotted as a function of H_{ext} in Fig. S6(b). The colored lines represent contributions from

different components. Thermoelectric signals in Pt/CoFeB are sufficiently small compared to the signal due to SOT. Figure S6(c) shows the damping-like spin Hall efficiency ξ_{DL} and the spin Hall conductivity σ_{SH} plotted as a function of temperature. We find $\xi_{\mathrm{DL}}{\sim}0.06$ at room temperature, corresponding to $\sigma_{\mathrm{SH}}{\sim}$ 650 $(\hbar/e)\Omega^{-1}\mathrm{cm}^{-1}$. ξ_{DL} and σ_{SH} slightly increase with increasing temperature, consistent with previous results obtained in similar heterostructures (Pt/Py) evaluated using the spin-torque ferromagnetic resonance (ST-FMR) technique[67] and lateral spin valve measurements[58].

Section S7. The efficiency of BiSb SOT

Although BiSb exhibit a large spin Hall efficiency, its resistivity is larger than typical metals, including the ferromagnetic metals that are used when forming SOT devices. Here we estimate the critical current needed to control the magnetization direction of the adjacent ferromagnet using BiSb and compare it with other materials. We consider a bilayer composed of a ferromagnetic metal (FM) layer and a non-magnetic metal (NM) layer, i.e. the latter generates spin current via the spin Hall effect. The critical current density is defined as the NM layer charge current density j_{NM} required to generate sufficient damping-like SOT to induce switching of the FM layer magnetization. In the macrospin limit, j_{NM} takes the form[68]

$$j_{\mathrm{NM}} = \frac{eH_{\mathrm{K,eff}}M_{\mathrm{s}}t_{\mathrm{FM}}}{2\hbar\xi_{\mathrm{DL}}}f(h_x) \tag{S11}$$

where $H_{\mathrm{K,eff}}$ is the effective anisotropy field, M_{s} is the saturation magnetization of the FM layer, and $f(h_x)$ is a function of $h_x \equiv \frac{H_x}{H_{\mathrm{K,eff}}}$. H_x is the external in-plane field H_x, e and $\hbar$ are the electric charge and the reduced Planck constant, respectively. Here we have assumed a perpendicularly magnetized system to estimate the switching current; however, the only factor that is relevant in the following discussion is the spin Hall efficiency ξ_{DL}. For simplicity, we assume the properties of the FM layer do not depend on the NM layer. The resistivity of the NM and FM layers are defined as ρ_{NM} and ρ_{FM}, respectively. Assuming a parallel circuit, the overall current that flows in the bilayer when j_{NM} is applied to the NM layer is given as

$$I_{\mathrm{c}} = j_{\mathrm{NM}}w\frac{\rho_{\mathrm{NM}}t_{\mathrm{FM}} + \rho_{\mathrm{FM}}d_{\mathrm{NM}}}{\rho_{\mathrm{FM}}} \tag{S12}$$

where w is the width of the device, which we assume is the same for both NM and FM layers. To compare the efficiency of BiSb with other materials system, we substitute typical values

of the relevant parameters and estimate I_c. We compare BiSb/CoFeB with W/CoFeB[69], the latter being the prototype of SOT-MRAM[70]. The parameters assumed are: $t_{\mathrm{CoFeB}} = 1$ nm and $\rho_{\mathrm{CoFeB}} = 150$ $\mu\Omega$cm for FM=CoFeB, $d_{\mathrm{W}} = 5$ nm, $\rho_{\mathrm{W}} = 120$ $\mu\Omega$cm, $\xi_{\mathrm{DL,W}}$=0.3 for NM=W, and $d_{\mathrm{BiSb}} = 10$ nm, $\rho_{\mathrm{BiSb}} = 1000$ $\mu\Omega$cm, $\xi_{\mathrm{DL,BiSb}}$=1.2 for NM=BiSb. The ratio of the critical current becomes

$$\frac{I_{\mathrm{c,W}}}{I_{\mathrm{c,BiSb}}} = \frac{\xi_{\mathrm{DL,BiSb}}}{\xi_{\mathrm{DL,W}}} \frac{\rho_{\mathrm{W}} t_{\mathrm{CoFeB}} + \rho_{\mathrm{CoFeB}} d_{\mathrm{W}}}{\rho_{\mathrm{BiSb}} t_{\mathrm{CoFeB}} + \rho_{\mathrm{CoFeB}} d_{\mathrm{BiSb}}} \sim 1.4. \tag{S13}$$

Thus we find the large spin Hall efficiency of BiSb is beneficial for SOT-MRAM even for its large resistivity: the current can be reduced by $\sim$40% compared to the state of art materials system, W/CoFeB.

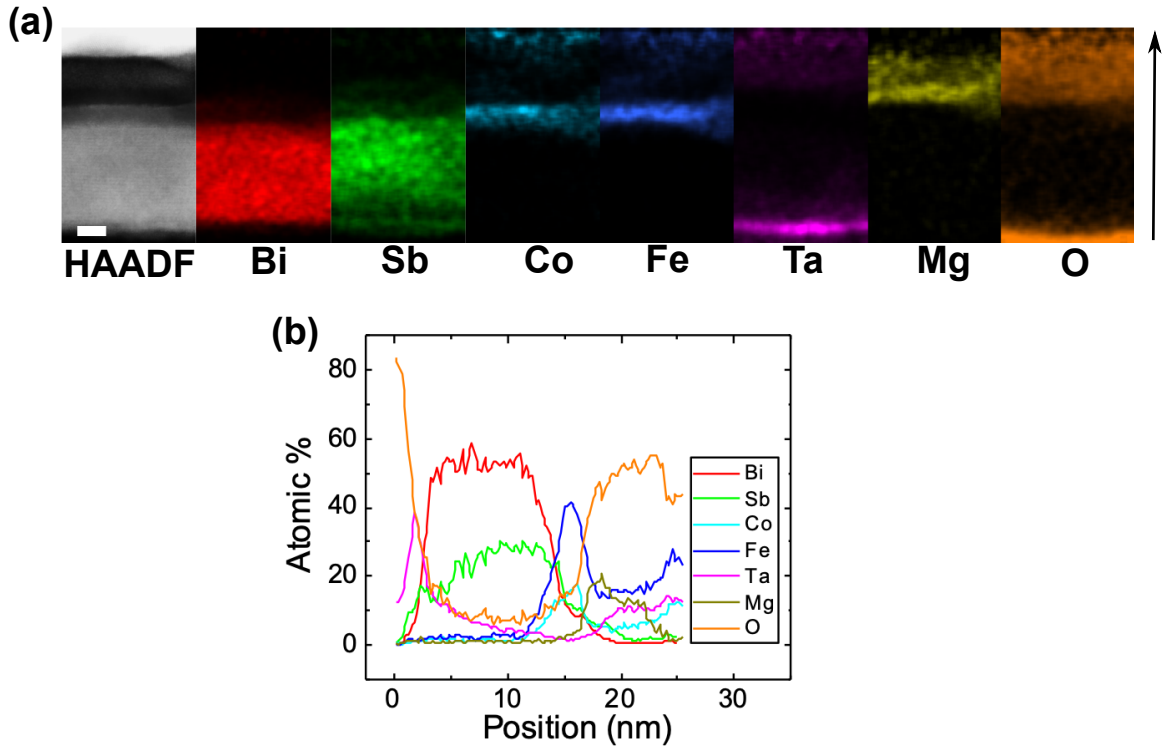

Fig. S1.HAADF-STEM and EDS mapping. (a) HAADF-STEM and elemental EDS maps of a heterostructure with 10.9 $Bi_{0.53}Sb_{0.47}$/2 CoFeB. The length of the horizontal white bar corresponds to ∼2 nm in the image. (b) Position dependence of the atomic ratio for different elements. The black arrow in (a) indicates the direction of the line scans. Position zero corresponds to the substrate/heterostructure interface.

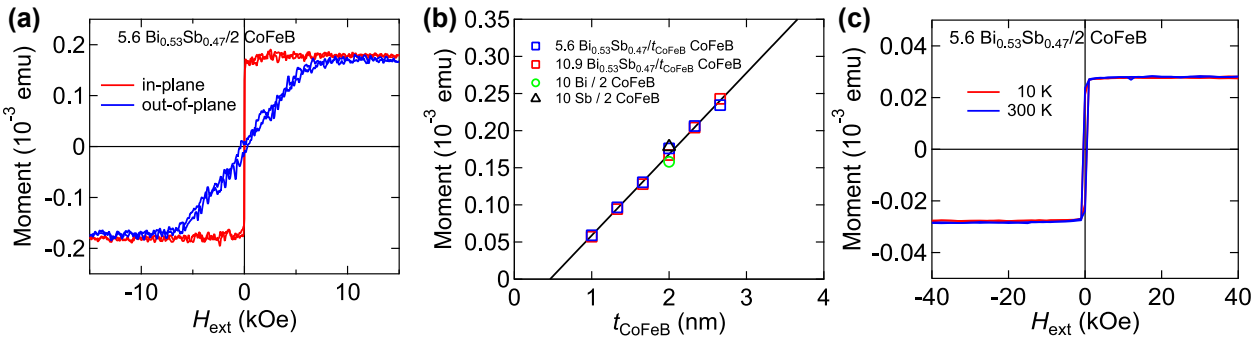

Fig. S2. Saturation magnetization and magnetic dead layer thickness. (a) Magnetization hysteresis loops of a heterostructure with 5.6 $Bi_{0.53}Sb_{0.47}$/2 CoFeB. The red and blue lines show the hysteresis when the field is applied along and normal to the film plane, respectively. (b) CoFeB thickness dependence of the saturated magnetic moment for heterostructures with 5.6 $Bi_{0.53}Sb_{0.47}/t_{CoFeB}$ CoFeB (blue squares) and 10.9 $Bi_{0.53}Sb_{0.47}/t_{CoFeB}$ CoFeB (red squares). The solid line represents linear fit to the data. The slope and the x-axis intercept of the linear line allows one to determine the saturation magnetization and the magnetic dead layer thickness, respectively. Data from heterostructures with 10 Bi/2 CoFeB and 10 Sb/2 CoFeB are laid together using green circle and black triangle, respectively. (c) In-plane magnetization hysteresis loops of a heterostructure with 5.6 $Bi_{0.53}Sb_{0.47}$/2 CoFeB. The red and blue lines represent hysteresis loops obtained at measurement temperatures of 10 K and 300 K, respectively. The results shown in (a) and (b) are obtained using VSM: the specimen film area is $\sim$9.6$\times$9.6 mm^2. SQUID is used to obtain the results shown in (c): the specimen film area is roughly 2$\times$6 mm^2.

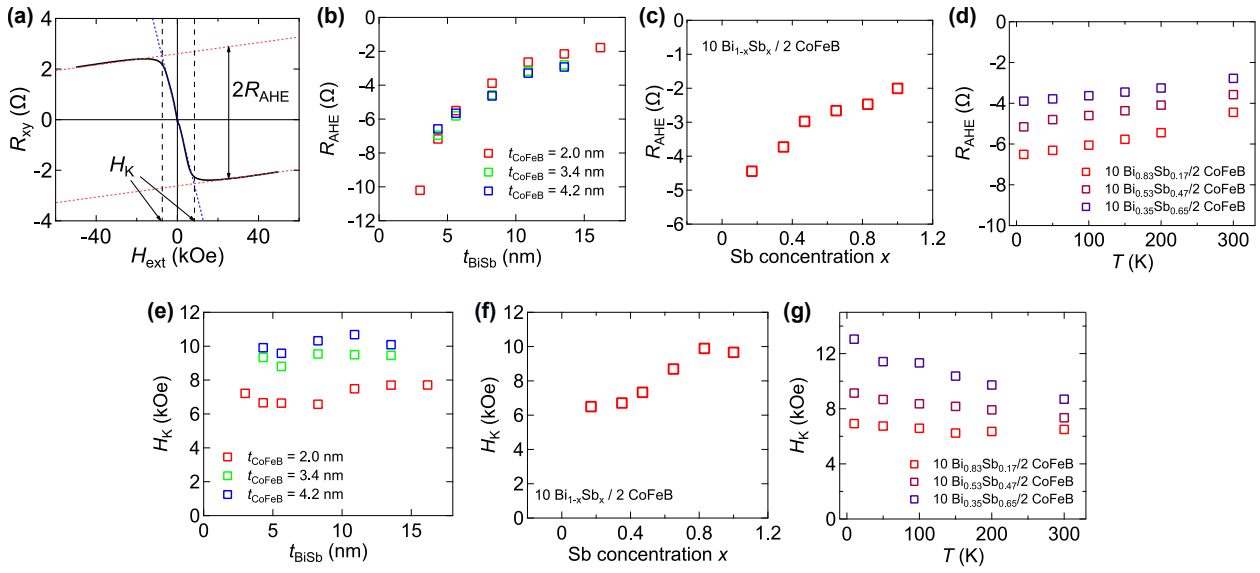

Fig. S3. Anomalous Hall resistance and anisotropy field. (a) Hall resistance R_{xy} of a heterostructure with 10.9 $Bi_{0.53}Sb_{0.47}$/2 CoFeB plotted as a function of magnetic field H_{ext} along the film normal (along the z-axis). Red and blue dashed lines show linear fits to the data in the high-field and low-field ranges, respectively. Definitions of the anomalous Hall resistance R_{AHE} and the anisotropy field H_{K} are illustrated in the panel. (b-g) R_{AHE} and H_{K} of heterostructures with t_{BiSb} $Bi_{1-x}Sb_x/t_{\mathrm{CoFeB}}$ CoFeB plotted as a function of $Bi_{1-x}Sb_x$ thickness t_{BiSb} (b,e), Sb concentration x (c,f) and the measurement temperature T (d,g).

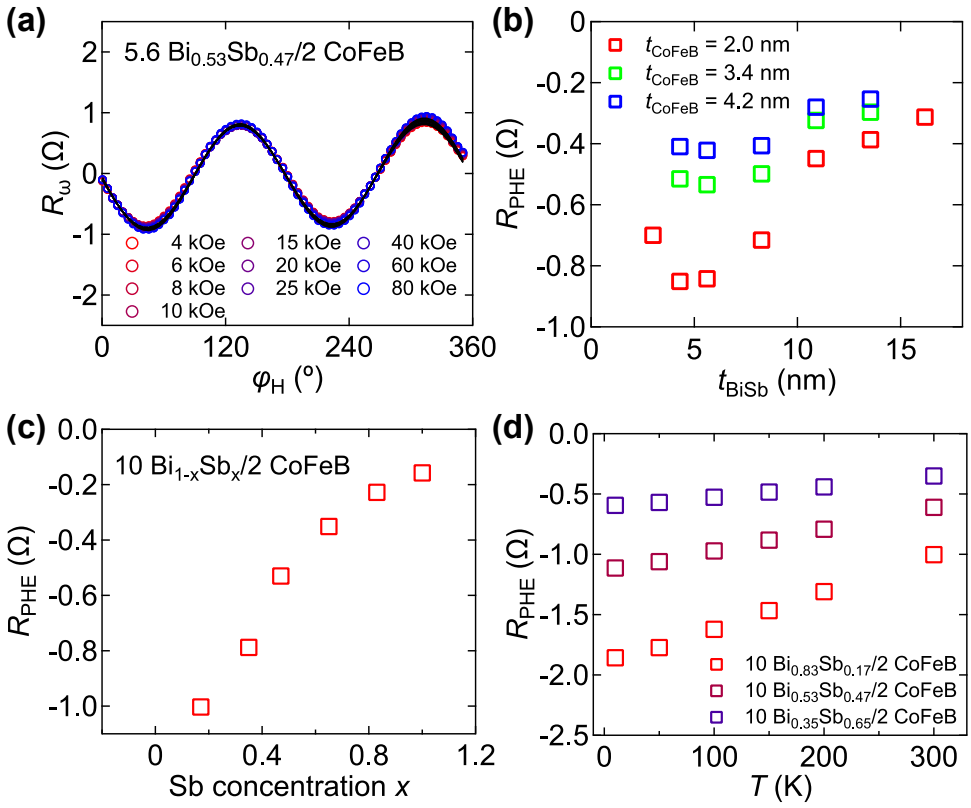

Fig. S4. First harmonic Hall resistance. (a) Field angle φ_{H} dependence of the first harmonic Hall resistance $R_{1\omega}$ of a heterostructure with 5.6 $Bi_{0.53}Sb_{0.47}$/2 CoFeB. Different symbols represent results obtained from various strengths of in-plane magnetic field. The black lines show the fitting with Eq. (S4). (b-d) Planar Hall resistance R_{PHE} plotted against $Bi_{1-x}Sb_x$ thickness t_{BiSb} (b), Sb concentration x (c) and the measurement temperature T (d), respectively.

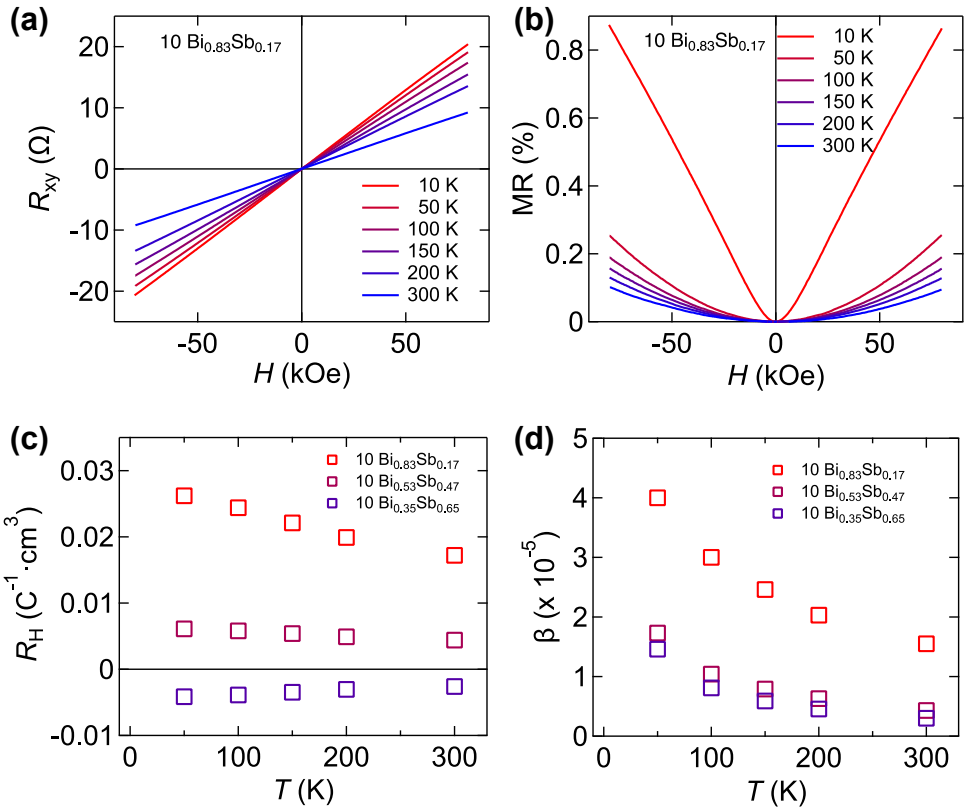

Fig. S5. Temperature dependence of magnetotransport properties of $Bi_{1-x}Sb_x$. (a-b) Temperature dependence of R_{xy} (a) and the magnetoresistance (MR) (b) plotted against external field H_{ext} along z for a heterostructure with10 $Bi_{0.83}Sb_{0.17}$ (without the CoFeB layer). (c,d) Hall coefficient R_H (c) and MR coefficient β (d) for $Bi_{1-x}Sb_x$ heterostructures (without the CoFeB layer) of different compositions plotted as a function of temperature.

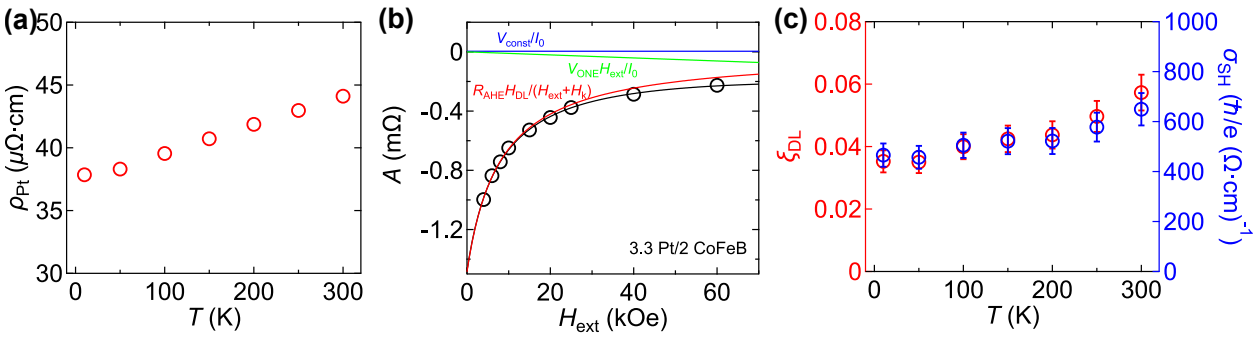

Fig. S6. SOT measurements of a standard sample: Pt/CoFeB. (a-c) The film structure is Sub./1 Ta/3.3 Pt/2 CoFeB/2 MgO/1 Ta (thicknesses in nm). (a) Temperature dependence of the Pt layer resistivity ρ_{Pt}. (b) H_{ext} dependence of fitting parameter A obtained at measurements carried out at room temperature. (c) Temperature dependence of the damping-like spin Hall efficiency ξ_{DL} and the spin Hall conductivity σ_{SH}.